APL Photonics

Anti-reflective surfaces: Cascading nano/microstructuring

Cite as: APL Photonics 1, 076104 (2016); https://doi.org/10.1063/1.4964851
Submitted: 14 April 2016 • Accepted: 03 October 2016 • Published Online: 18 October 2016

Yoshiaki Nishijima, Ryosuke Komatsu, Shunsuke Ota, et al.

Anti-reflective surfaces: Cascading nano/microstructuring

Yoshiaki Nishijima,[1,a] Ryosuke Komatsu,[1] Shunsuke Ota,[1]
Gediminas Seniutinas,[2] Armandas Balčytis,[2,3] and Saulius Juodkazis[2,b]
[1]*Department of Electrical and Computer Engineering, Graduate School of Engineering, Yokohama National University, 79-5 Tokiwadai, Hodogaya-Ku, Yokohama 240-8501, Japan*
[2]*Centre for Micro-Photonics, Faculty of Engineering and Industrial Sciences, Swinburne University of Technology, Hawthorn, VIC 3122, Australia*
[3]*Institute of Physics, Center for Physical Sciences and Technology, 231 Savanorių Avenue, LT-02300 Vilnius, Lithuania*

(Received 14 April 2016; accepted 3 October 2016; published online 18 October 2016)

The creation of anti-reflective surfaces is reliant on the engineering of the surface textures and patterns to enable efficient trapping or transmission of light. Here we demonstrate anti-reflective layers composed of hierarchical nano/microscale features that are prepared on Si using a combination of wet and dry etching processes, and which are both scalable and affordable. The performance of the structured surfaces was tested through optical measurements of the reflectance, transmittance, and scattering spectra from the visible to mid-infrared wavelength regions, and the results were verified using numerical simulations to identify the performance of the textured anti-reflective layers. The anti-reflective properties of the layers were shown to be dramatically improved by the composite nanostructured surfaces over a broad spectral range, which thus provides a basis for the design rules that are essential for the progress towards effective anti-reflector fabrication. At normal incidence, the hierarchical surfaces achieve reflectances that are 10–80 times lower than that of conventional single-etch nano-microstructures. Portions of the absorbed, transmitted, scattered, and reflected light in the visible-IR spectrum are presented to illustrate the results. [http://dx.doi.org/10.1063/1.4964851]

I. INTRODUCTION

Control of the anti-reflective properties of semiconductor surfaces, preferably based on the use of existing semiconductor processing techniques or self-assembly methods, is being vigorously pursued for use in solar cell applications,[1–5] where hierarchical structures in particular have demonstrated superior performance.[6,7] In addition, these surfaces are required for other uses, including displays, optical lenses, and defense applications, which would benefit from suppressed reflectance.[8–13] One often overlooked but important benefit that these hierarchical nano/microstructures bring to anti-reflective surface applications is their applicability over very wide-ranging spectral windows, because they have a lower angular dependence of reflectivity (i.e., a higher omnidirectionality) than is typical for such multilayered dielectric films.[14–16]

One of the most versatile and effective of the current anti-reflective surfaces is black silicon (b-Si), which uses an anti-reflective surface layer of randomly arranged sub-wavelength-sized conical Si nanospikes (Fig. 1(a)). These nanofeatures act as light couplers that offer a gradual refractive index transition from the air to semiconductor.[17,18] In solar cells, a b-Si device layer has been shown to provide a high conversion efficiency of 22.1%.[19] In addition to its uses in conventional photovoltaic methods, b-Si is also effective for use in light energy harvesting based

[a]nishijima@ynu.ac.jp
[b]sjuodkazis@swin.edu.au

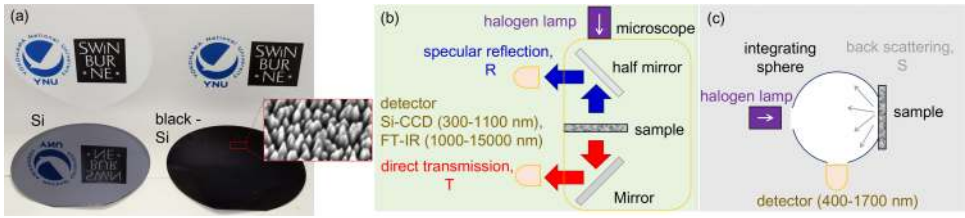

FIG. 1. (a) Photograph of a mirror Si surface and an anti-reflective black-Si (b-Si) surface. The inset shows a scanning electron microscope (SEM) image of the b-Si surface. (b) Schematic illustration of the setup used to measure specular reflectance R and direct transmission T with the microscopic system, and (c) the setup used to measure back scattering S with an integrating sphere.

on thermo-photovoltaic generation, and particularly in harnessing the infrared part of the solar spectrum to boost the total achievable efficiency. It was previously demonstrated how inductively coupled plasma reactive ion etched (ICP-RIE) b-Si with plasmonic nanoparticles can be used as a highly effective absorber for photo-thermoelectric conversion applications.[20] Nanospikes of b-Si coated with Au have shown high performance when used in surface-enhanced Raman spectroscopy/scattering (SERS)[21] and were also proven to be bactericidal through the mechanical destruction of bacterial membranes.[22] Using a simple chemical treatment in either gas phase or solution, these nanotextured surfaces can also be rendered super-hydrophobic.[23,24]

The spectral performance and the anti-reflective properties of b-Si can be altered by varying the ICP-RIE etching regimes to cause modifications in the size, shape, and separation of nanospikes.[25] However, these single-step etching routines result in nanotexturing with a fairly narrow geometric parameter distribution, which in turn precludes broadband performance. Further control over the optical properties of these surfaces therefore requires a hierarchical approach that combines two or more different nano/microstructuring techniques.[7,26] Additionally, to provide meaningful differentiation among the performance levels of the various anti-reflective layers, it is important to provide an analysis that goes beyond a basic treatment of the total reflectance by measuring the constituent specular and diffuse reflectance components of the layers and their total transmittance; then, based on these values, the absorbance of the layers can be deduced over the entire relevant wavelength region (from visible to mid-infrared).

Here we show how anti-reflective surfaces that provide high suppression of specular reflectivity and that are unrivaled in the breadth of their spectral range can be produced by superimposing plasma-etched nanospike structures on a microtextured surface created by wet etching.

II. EXPERIMENTAL

A. Nanotextured Si

The composite micro/nanostructured surfaces were prepared by a combination of disparate etching steps — including alkaline wet etching, metal assisted hydrofluoric (HF) acid etching, and RIE — to prepare micropyramidal, nanowire, and nanospike Si structures, respectively.

The micropyramidal structures were fabricated by alkaline wet etching using a commercially available NaOH solution (Pure Etch T501S, Hayashi Pure Chemical, Osaka, Japan), which was diluted in ion exchanged water to a concentration of 0.5M (~12 wt. %). The 3-in.-diameter ⟨100⟩ surface orientation Si wafer was dipped in the etching solution at 80 °C for 10 min. In the specific case of subsequent fabrication of high aspect ratio nanowires, larger micropyramids were required; therefore, longer etching times that ranged from 48 to 72 h at room temperature (RT) were used.

The nanospike structures were fabricated using an ICP-RIE tool (RIE-101iPH, Samco, Kyoto, Japan) with the plasma composed of a 35 SCCM SF_6 and 45 SCCM O_2 flow rate gas mixture. The ICP power was maintained at 150 W and the RIE bias was 15 W, with back-pressure of 1 Pa. After the RIE process, the substrates were washed for 5 min in a 10 wt. % solution of H_2SO_4 to strip off any residual traces of the self-assembled fluoropolymer etch mask.

The nanowire structures were fabricated by metal-assisted etching,[27–30] which involved dipping the Si into a 0.02M $AgNO_3$ and 0.2M HF mixed solution at RT for 20 min.

B. Characterization

The spectral performance of the micro/nanotextured surfaces was characterized through the measurement of their specular reflectance (R) and direct transmittance (T) spectra, which were then used to deduce the total extinction ($E = 1 - R + T$). Extinction is defined as the removal of the optical power from an incident beam, where the optical power is the sum of the absorption and scattering of electromagnetic energy in the substrate. The scattering in turn is composed of diffuse back-reflection and diffuse transmission into the substrate. Therefore, because the 3D surface texturing produces both regular specular reflection and diffuse reflection of the light, the scattering spectra were measured to obtain an accurate estimate of the total absorbance. At longer wavelengths, where detector limitations prevent determination of the scattering, the term extinction is used.

The reflectance spectra of the anti-reflective surfaces were measured in the visible to near-infrared (IR) and mid-IR wavelength regions using micro-spectroscopic techniques. The visible to near-IR spectral acquisitions were performed using a combination of an inverted microscope (IX-71, Olympus, Tokyo, Japan), a halogen lamp and a fiber-coupled charge-coupled device (CCD) spectrometer (300-1100 nm, C10083CA, Hamamatsu Photonics, Shizuoka, Japan); the light collection ability was defined by the numerical aperture, $NA = 0.3$. For the mid-IR region, a Fourier transform spectroscopy system (1000-15 000 nm, FT-IR-4000, JASCO, Tokyo, Japan) with a microscope attachment that was equipped with a Cassegrain lens with $NA = 0.5$ (IRT-1000, JASCO, Tokyo, Japan) was used in both the transmittance and reflectance measurement configurations (Fig. 1(b)). Metal mirrors made from silver and gold (TFAG and TFG, Sigma Koki , Tokyo, Japan) were used as the high-reflectance references in the visible-to-near-IR and mid-IR spectral regions, respectively. The measured reflectance spectra were normalized with respect to the absolute reflectance values of the Au and Ag layers based on the specifications provided by the manufacturer for the range from 400 nm to 2000 nm. The longer wavelengths up to 15 000 nm were then extrapolated using the Drude model.[31,32] The reflection spectra of the reference mirrors are shown in the supplementary material. The setup used for the acquisition of the light scattering spectra comprised a 1.5-in.-diameter integrating sphere (Infragold GPS-IG, Labsphere, North Sutton, US) and a collimated halogen lamp that was used as a light source. The sample surface was oriented normal to the light flux and the scattered light was collected at a port located at 90° to both the sample and the light source ports using the CCD detector and an optical spectrum analyzer (400-1700 nm, Q8381A, Advantest, Tokyo, Japan), as shown in Fig. 1(c). Each of the optical measurements (for vis-NIR T and R, NIR-MIR T and R, and vis-NIR S) was performed using a specific optical setup.

C. Numerical modeling

The experimentally measured spectral characteristics of the anti-reflective surfaces are complicated by additional reflections from the opposite (nontextured) Si wafer surface. Numerical simulations were therefore conducted to isolate the behavior of the textured surfaces without including any residual effects of the fabrication methods. This then provides the ability to estimate the maximal achievable performance for any given texture.

Numerous disparate approaches have been used to simulate the optical properties of nanostructured anti-reflective surfaces.[33,34] Because the geometries of the structures under investigation are greatly different to previous structures and are not easy to approximate, the vectorial and time-dependent finite-difference time-domain (FDTD) method was selected to simulate all surfaces using the same numerical approach.

The FDTD simulations of the optical transmittance and reflectance were performed using commercially available solver software (Lumerical Solutions, Vancouver, Canada) on large 3D renderings of representative 10×7 μm^2 segments of the anti-reflective surfaces, and on a flat Si surface for reference. These dimensions were chosen for the simulation region because they represent the size and aspect ratio of the scanning electron microscope (SEM) images that provided the

best trade-off for the maximum area at a satisfactory resolution with suitable levels of noise for the 3D model reconstruction. A model of the NaOH-etched micropyramid-decorated structure was obtained via the random generation of pyramids on a planar surface. The pyramid parameters were deduced from the SEM images and were assumed to be normally distributed. The 3D rendering of the nanospike-covered b-Si surface was directly reproduced from a backscattered SEM image. The composite b-Si and micropyramid structure model was generated by overlaying the coordinates of the two corresponding individual models. A broadband pulsed plane wave source was used for optical excitation in the visible-to-near-IR spectral range. Simulations were conducted for two perpendicular incident light polarizations and the results were then averaged to obtain the response for unpolarized light. All simulation boundaries were terminated using perfectly matched layer boundary conditions.

The transmitted power is registered in the bulk Si at a level 2.5 μm below the structured layer. The transmittance values were subsequently recalculated by applying the Beer-Lambert law to add the absorption losses that are expected to occur in the 500 μm Si wafer thickness (which represents the wafers used in the experiments). The spectral dependence of the complex refractive index was taken into account on the basis of information reported in the literature.[35]

III. RESULTS AND DISCUSSION

A. One-step nano-texturing

SEM images that illustrate each of the fabricated single-etch derived surface 3D texture patterns are shown in Fig. 2. The micropyramidal structures that were created via alkaline wet etching (Fig. 2(a)) range from 2 to 10 μm in height, and thus are quite large in comparison to the wavelength of light in the visible-to-mid-IR range, and also have a low aspect ratio of ~0.8. Conversely, the nanowires (Fig. 2(c)) have exceptionally high aspect ratios of up to ~150 with the individual wires having thicknesses in the ~30-40 nm range and heights in excess of 5 μm. The b-Si surface (see Fig. 2(b)) is decorated with nanospikes that are ~100 nm wide and ~200-300 nm high; unlike the previous cases, this means that the nanotexturing is strictly sub-wavelength for the spectral range of interest in this study.

The optical reflectance spectra for these three basic structures are shown in Fig. 3. In the visible-to-near-IR spectral region, all three structures significantly reduce the surface reflectivity. The performance of the high-aspect-ratio Si nanowire layers is particularly notable because of the exceptional 0.3% reflectance throughout the wavelength range.

In contrast, in the mid-IR region, the reflectance begins to increase again at wavelengths greater than $\lambda = 2$ μm. Because the size of the nanospikes that comprise the b-Si surface is the smallest, this substrate is the first to lose its anti-reflective properties in the infrared range; however, it was demonstrated that the anti-reflective spectral region can be extended by varying the height of the microspikes.[25] The wet-etched micropyramid and nanowire structures show anti-reflective performance up to $\lambda = 7.5$ μm, with the former structure having greater randomness and thus exhibiting a more consistent spectral performance, whereas the nanowires show some interference-derived

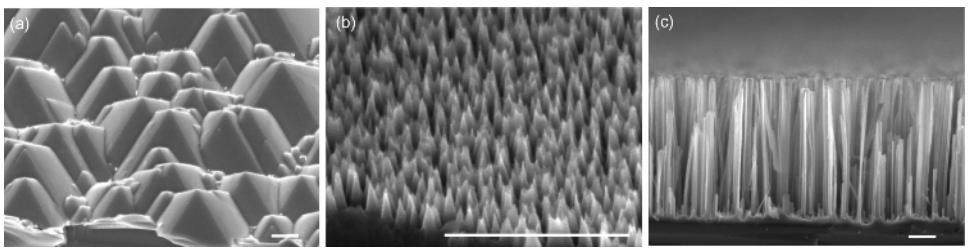

FIG. 2. SEM micrographs of the single-etch-step nanotextured Si surfaces that are used as constituent building blocks for the hierarchical anti-reflectors. (a) Si micropyramid textured surface formed by alkaline wet etching. (b) b-Si nanospikes fabricated by ICP-RIE etching. (c) Si nanowires formed by Ag-metal assisted HF etching. All scale bars represent 1 μm.

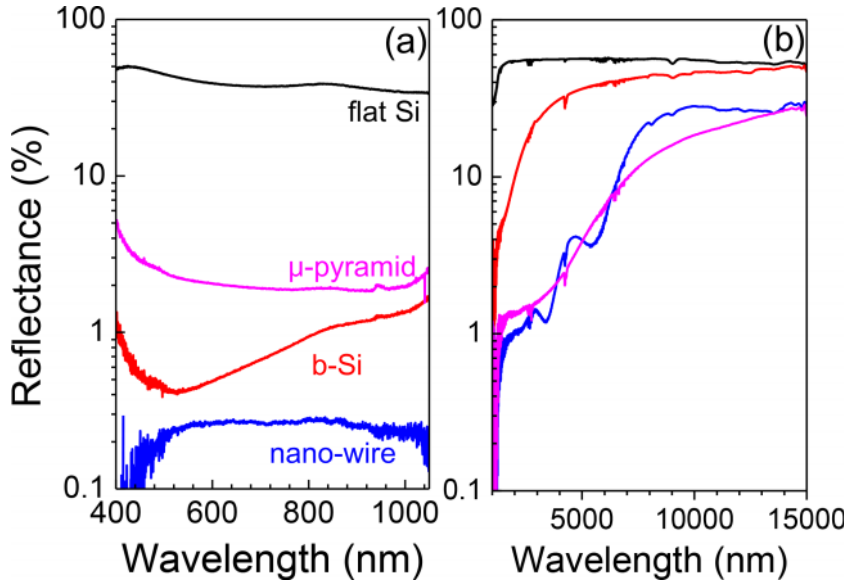

FIG. 3. Reflectance spectra of the mirror Si, μ-pyramid, b-Si nanospikes, and nanowire structures in the (a) visible and (b) NIR-to-MIR wavelength regions.

reflectance oscillations. The IR radiation is within the Si band gap, and thus the electromagnetic energy absorption within the semiconductor in this wavelength range is weak and mostly occurs because of free carrier absorption. Therefore, when the direct transmittance is high, the specular reflectance from the rear surface begins to play an important role. In this case, reflectance suppression is reliant on the scattering of light (by either forward-scattering into the substrate or back-scattering into the air).

B. Hierarchical nanotexturing

Using a combination of the different fabrication techniques, compound hierarchical nanotextured surfaces can be prepared. The nano/microcomposite structures that are reported here were prepared using the Si μ-pyramid decorated wafer as a base surface, on which a superstructure composed of either ICP-RIE b-Si nanospikes (Fig. 4(a)), or metal-mediated wet etching-derived nanowires (Fig. 4(b)) was then etched. Depending on the dry etching time used, the reactive ion etched b-Si nanospikes can range in average height from 200 to 700 nm (corresponding to etching durations in the range from 15 min to 45 min). However, longer ICP-RIE times, which were expected to yield ~1 μm nanospikes in a 60 min duration, resulted in the disappearance of the underlying micropyramidal pattern because of over-etching.

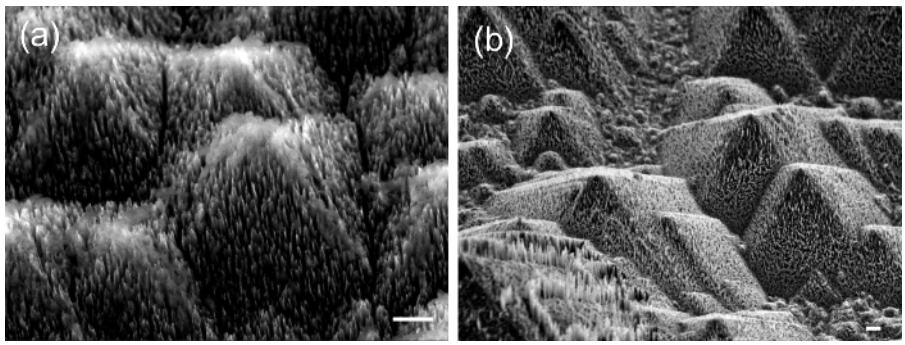

FIG. 4. SEM images of μ-pyramidal structures with superstructures of (a) b-Si nanospikes and (b) nanowires applied to their surfaces. The scale bars represent 1 μm.

The RIE etched b-Si nanospikes are formed because of spontaneous and self-regenerative masking that is a result of agglomeration of the nonvolatile chemical reaction products. However, metal-assisted wet etching begins by first creating deep holes in the substrate, which subsequently percolate and then create a densely packed random array of high-aspect-ratio Si nanowires. This method removes a great deal of the substrate material (up to a depth of ~5 μm, and thus significantly larger micropyramids are required to maintain the hierarchical structure. This was achieved using a more gradual alkaline etching process at room temperature over a longer period of time, which resulted in the fabrication of micropyramids that were 10-20 μm high. The individual sets of physical and chemical parameters and the etching time can all be adjusted independently, which means that this method provides greater control over the properties of the resulting anti-reflective surfaces. Additionally, the fabrication was performed at the 3 in. wafer scale. Micropyramidal etching and b-Si formation can thus be accomplished with high structural size distribution uniformity and this allows similar reflectance performance to be obtained over the entire wafer. However, nanowire formation by metal-assisted etching requires careful control of the reaction rate. The brittle nature of these narrow high-aspect-ratio structures provides a particular challenge for rinsing and drying processes on the wafer scale.

The reflectance spectra of the nano/microcomposite anti-reflective surfaces in the visible-IR spectral regions are shown in Fig. 5. Both of the combined structures show less than 1% reflectance for visible wavelength light at normal incidence. The micropyramids decorated with b-Si nanospikes show exceptional reflectance performance, with 80 times lower reflectance than the micropyramids alone and 10 times lower reflectance than the b-Si nanospikes alone. In the mid-IR range, (see Fig. 5), enhanced suppression of the reflected light in comparison to that of the single-etch-step structures is also observed, with the reflectance not exceeding 10% throughout. The spectra from the composite surfaces are qualitatively similar, with the sole difference being that the b-Si superstructure-decorated surface shows increased performance in the near-IR range at the cost of reduced reflectivity suppression in the mid-IR range, whereas the pyramidal/nanospike surface demonstrates intermediate reflectance throughout. In either case, the composite anti-reflective surfaces significantly outperform any of their single-etch-step counterparts. These results clearly show that the hierarchical nano/microcomposite structures extensively reduce surface reflectivity. This knowledge is useful for the solar cell design because it enables mitigation of the losses associated with reflection, which is a limiting factor for the conversion efficiency.

The reflectivity is contingent on both the scattering at the surface and the absorption of light by the substrate material. The scattering cross section is dependent on the size and shape of the texture

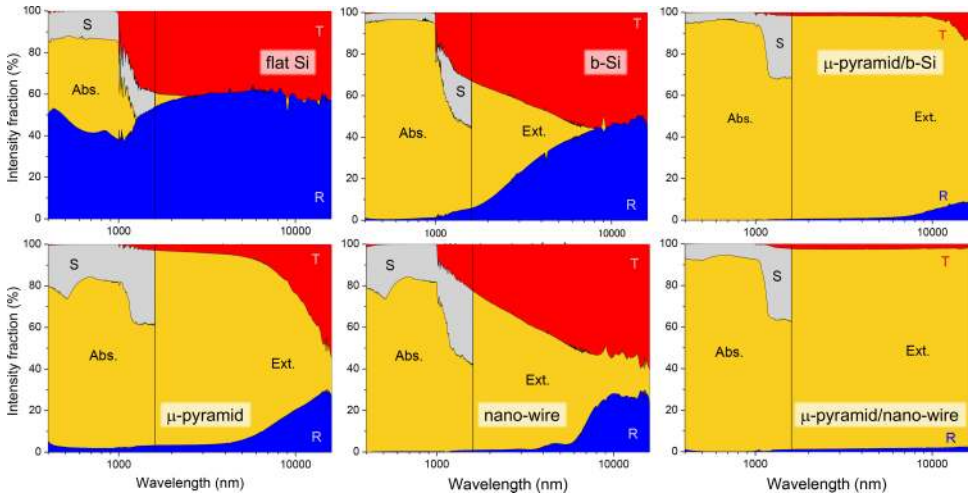

FIG. 5. Experimentally measured fractions of the reflectance, absorbance, transmittance, and extinction combined over the vis-IR spectral ranges from flat Si (mirror surface) and five different nanotextured surfaces (see the text for details of these surfaces).

features and the wavelength of the incident light. Dimensions of the structures of the order of a particular wavelength tend to effectively scatter that light, which thus increases the potential number of light-matter interaction events. Additionally, if the dimensions of the gaps that separate such structures are also of the same order of magnitude as the wavelength, the electromagnetic energy can be localized and accumulated there, thus further aiding in the absorption process. However, while all scattering suppresses the specular reflections, only the light that is scattered into or is in the immediate vicinity of the substrate contributes to the enhanced absorption. Therefore, to understand the underlying reasons for the anti-reflective performances of the surfaces under consideration in this work, it is important to discriminate between the light that is scattered into the air and the light that is scattered into the semiconductor material.

Figure 5 shows the optical transmittance spectra at normal incidence for all the anti-reflective surfaces, which, in the IR wavelength region and beyond the Si absorption band, are roughly equivalent to the fraction of the electromagnetic radiation that is scattered into the substrate. Notably, the micropyramid patterned surfaces, including the micro/nanocomposites containing nanowires and b-Si, show the lowest transmittance values. The planar nanowire, b-Si nanospikes, and flat Si wafer surfaces show higher transmittance values in that order. In contrast, Fig. 5 also shows the scattering intensity ratio that was measured using an integrating sphere, and this ratio is proportional to the fraction of light that is diffusely back-scattered into the air. It is evident that for wavelengths beyond $\lambda = 1100$ nm, all types of texturing increase the scattering, with the micropyramids having the strongest effect. In the near-IR region (beyond the Si band gap), the sum of transmitted, reflected, and scattered light is nearly equal to 100% for all surfaces under study. These findings therefore indicate that while surface texturing does cause reflection to decrease in the near-IR region, most of the light is not absorbed, but is either transmitted or scattered. However, the composite micropyramidal surfaces with etched-in nanowires or b-Si nanospikes show almost 100% light absorption in the UV to visible wavelength regions.

The lowest reflectivity was measured from the surfaces of the micropyramids that were covered with the b-Si spikes (Fig. 5) and was more than 10 times below the level achieved using single-etch texturing, depending on the b-Si treatment time (and the resulting height of the nanospikes). Reflectance suppression could be further enhanced via the application of an overlaid SiN or SiO_2 film, which would mediate between the low refractive index of air and the high refractive index of Si, while also forming quarter-wavelength interference coatings for specific wavelengths.[36] One added benefit of this type of film is that it also reduces surface recombination, which is important in solar energy harvesting applications.[37] Similarly, nanotextured light trapping structures that were created using metal-assisted etching have been used successfully at the rear side of a solar cell, with a thin atomic layer deposited ZnO overlayer separating the Si surface from the electrode and acting as a tunnel oxide-passivated contact.[38]

C. Numerical modeling

The FDTD simulations that were conducted on the composite b-Si nanospike and nanowire decorated micropyramids and the constituent micropyramids, nanowires, and nanospikes themselves (along with the flat Si surface for reference) corroborate the experimental findings, as demonstrated by the numerically modeled single-boundary reflectance and transmittance spectra shown in Fig. 6. The experimentally measured reflectance and transmittance spectra are influenced by the reflections from the opposite (nontextured) Si wafer surface. Therefore, while their results are not directly comparable with those of the experiments, the single-boundary simulations provide complimentary information on the behavior of a given topology. However, because of the computationally limited size of the simulated Si volume and the limited sampled areas of the random surfaces, and because the rear-side surface reflection is disregarded, the numerical simulations predict higher transmittance values than those observed experimentally. Additionally, some discrepancies in the transmittance results between the simulations and the experiments are observed for both the b-Si spikes and the nanowires when compared with the flat Si surface, because the transmission through the flat Si was stronger in the experiments. In addition, the simulations in the 0.4 μm–2 μm wavelength range predict that the flat nanowire surfaces will yield superior anti-reflective properties.

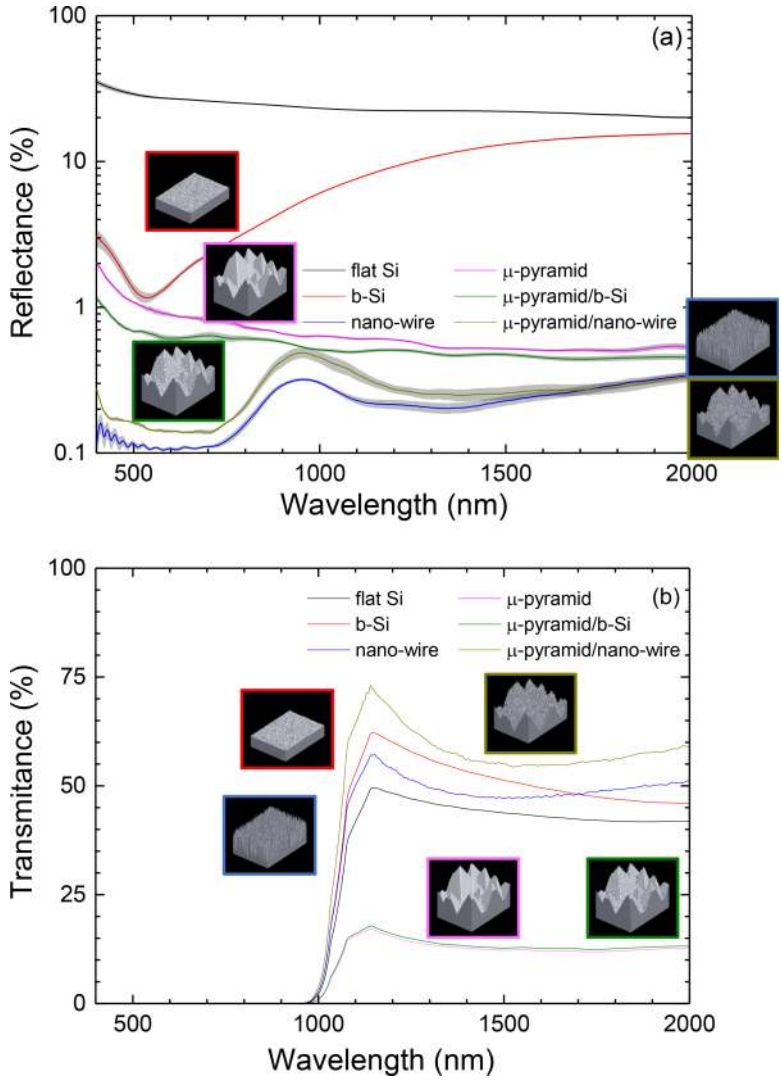

FIG. 6. FDTD simulation results for surface textured samples. Simulated (a) reflectance and (b) transmittance spectra of nanotextured surfaces; note the logarithmic scale used for R here. Numerical errors due to high-frequency noise are highlighted by the grey region along the line in (a). 3D renderings of the surfaces under numerical investigation, i.e., planar b-Si, NaOH etched micropyramids, composite micropyramid/b-Si surfaces, which were made using SEM data (the pictorial markers represent the patterns used in the simulations; see the text for full details). Silicon optical constants taken from the Lumerical database were used.

One possible reason for the deviations between the experiments and the simulations is that in the experiments, there was a limitation to the transmission and reflection collection efficiency that was imposed by the numerical apertures of the lenses used ($NA = 0.3$ for visible and $NA = 0.5$ for IR), while in the simulations, all the light intensity is captured by a suitable close placement of the monitors relative to the surface ($NA \rightarrow 1$). However, this provides a good way to determine the part of the anti-reflective effect that is due to scattering of the light into the Si substrate at various obtuse angles (i.e., the light that is trapped in the substrate and thus cannot be measured directly). Placement of the transmittance monitor close to the textured surface allows it to capture both the directly transmitted and scattered light. In contrast, the opposing Si surface prevents the transmission of most of the forward-scattered light so that it cannot be detected experimentally. In this context, it is unsurprising that the plain micropyramid structures show the lowest transmission because of the dominant in-plane scattering. Additional nanotexturing of the pyramids broadens the range of k-vectors at which the light is scattered, and thus increases the simulated near-field transmission,

with the nanowire decoration effect being most prominent. Also, the simulated transmittance values for the single-step-textured b-Si and nanowire surfaces are higher than those for flat Si, whereas the experimental measurements show that texturing suppresses the transmittance. This illustrates an important concept: that nanotexturing aids in the coupling of light into the substrate, but does so at the cost of the transmittance.

Another possible reason for the mismatch between the results of the theory and those of the experiments is the definition of the light source in FDTD, which causes coherent addition of the fields[39] and makes the readout of the local light field intensity sensitive to minor changes in the monitoring location. To overcome this issue, it would be necessary to perform multiple simulations using different random samples of the same surface along with different placements of the light source and different average intensities; this is planned to be done as part of our future work.

As mentioned previously, when the structures that comprise the nanotexture are comparable in size to the wavelength, as in the cases of the nanospikes and the nanowires, they strongly scatter and absorb that light. Additionally, if these structures are sub-wavelength in scale, the light perceives them as an effective index medium that eases the coupling of electromagnetic energy from the air to the semiconductor and vice versa. However, the interaction of the comparatively large micropyramids with visible light can be accounted for using a ray optics approximation, and is thus shown to mostly contribute to the scattering. However, angled reflections off the pyramidal faces can be beneficial when these faces have been decorated using sub-wavelength structures such as nanowires and nanospikes because this allows multiple light-matter interactions. Additionally, the increased surface area can support a higher nanoscale feature density and thereby offers increased absorbance and an extremely suppressed reflectance.

IV. CONCLUSION AND OUTLOOK

It has been demonstrated that hierarchical nanotexturing of Si surfaces effectively reduces the surface reflectivity to more than 10 times below that of typical single-etch step nano/microstructures over the visible wavelength region at normal incidence. Numerical modeling of the reflectance, transmittance, and extinction based on the patterns that were obtained from SEM imaging qualitatively describes the optical performance of these hierarchical nanotextured surfaces well. Production of the hierarchical random nanoscale patterns that are fabricated on Si is both simple and scalable. The resulting surfaces can be used in large surface area applications and can serve as templates for replication of the nanotexture for numerous applications in rapidly evolving fields such as super-capacitors, electrodes, and optical coatings. Light extraction surfaces for light-emitting diodes and for the control of surface emissivity represent another potential field of applications to add to use in photovoltaics, thermovoltaics, black body light sources, and broadband reflectance suppression coatings;[20,40] all these structures can benefit from hierarchical patterns of nano-microscale structures.

SUPPLEMENTARY MATERIAL

See the supplementary material for the reflection spectra of the reference Au and Ag mirrors.

ACKNOWLEDGMENTS

Y.N. is grateful for the partial support provided by the Japan Society for the Promotion of Science (JSPS), the Grants-in-Aid for Scientific Research, the Open Partnership Joint Projects of JSPS Bilateral Joint Research Projects, and the Tateishi Foundation. S.J. is grateful for partial support via the Australian Research Councils No. DP130101205 Discovery project. The FDTD simulation work was performed on the swinSTAR supercomputer at Swinburne University of Technology. The authors are also grateful for the start-up funding and the support of the Nanotechnology facility at Swinburne.

[1] N. Yamada, T. Ijiro, E. Okamoto, K. Hayashi, and H. Masuda, "Characterization of antireflection moth-eye film on crystalline silicon photovoltaic module," Opt. Express **19**(S2), A118–A125 (2011).
[2] P. Gao, J. He, S. Zhou, X. Yang, S. Li, J. Sheng, D. Wang, T. Yu, J. Ye, and Y. Cui, "Large-area nanosphere self-assembly by a micro-propulsive injection method for high throughput periodic surface nanotexturing," Nano Lett. **15**(7), 4591–4599 (2015).
[3] P. Gao, H. Wang, X. Sun, W. Han, J. Li, and J. Ye, "Efficient light trapping in low aspect-ratio honeycomb nanobowl surface texturing for crystalline silicon solar cell applications," Appl. Phys. Lett. **103**, 253105 (2013).
[4] Z. Yang, X. Li, S. Wu, P. Gao, and J. Ye, "High-efficiency photon capturing in ultrathin silicon solar cells with front nanobowl texture and truncated-nanopyramid reflector," Opt. Lett. **40**(6), 1077–1080 (2015).
[5] A. Ingenito, O. Isabella, and M. Zeman, "Nano-cones on micro-pyramids: Modulated surface textures for maximal spectral response and high-efficiency solar cells," Prog. Photovoltaics: Res. Appl. **23**, 1649–1659 (2015).
[6] M. Otto, M. Algasinger, H. Branz, B. Gesemann, T. Gimpel, K. Füchsel, T. Käsebier, S. Kontermann, S. Koynov, X. Li, V. Naumann, J. Oh, A. N. Sprafke, J. Ziegler, M. Zilk, and R. B. Wehrspohn, "Black silicon photovoltaics," Adv. Opt. Mater. **3**(2), 147–164 (2015).
[7] F. Toor, H. M. Branz, M. R. Page, K. M. Jones, and H.-C. Yuan, "Multi-scale surface texture to improve blue response of nanoporous black silicon solar cells," Appl. Phys. Lett. **99**, 103501 (2011).
[8] H. K. Raut, V. A. Ganesh, A. S. Nairb, and S. Ramakrishna, "Anti-reflective coatings: A critical, in-depth review," Energy Environ. Sci. **4**, 3779 (2011).
[9] T. Takamasa, U. Makoto, K. Yamada, Y. Tanaka, K. Kintaka, H. Kasa, and J. Nishii, "Fabrication of antireflective subwavelength structure on spherical glass surface using imprinting process," Appl. Phys. Express **3**, 112501 (2010).
[10] K.-C. Park, H. J. Choi, C.-H. Chang, R. E. Cohen, G. H. McKinley, and G. Barbastathis, "Nanotextured silica surfaces with robust superhydrophobicity and omnidirectional broadband supertransmissivity," ACS Nano **6**(5), 3789–3799 (2012).
[11] D. Infante, K. W. Koch, P. Mazumder, L. Tian, A. Carrilero, D. Tulli, D. Baker, and V. Pruneri, "Durable, superhydrophobic, antireflection, and low haze glass surfaces using scalable metal dewetting nanostructuring," Nano Res. **6**, 429–440 (2013).
[12] S. R. Kennedy and M. J. Brett, "Porous broadband antireflection coating by glancing angle deposition," Appl. Opt. **42**(22), 4573–4579 (2003).
[13] T. Yanagishita, T. Kondo, K. Nishio, and H. Masuda, "Optimization of antireflection structures of polymer based on nanoimprinting using anodic porous alumina," J. Vac. Sci. Technol., B: Microelectron. Nanometer Struct.–Process., Meas., Phenom. **26**, 1856–1859 (2008).
[14] Y.-T. Lu and A. R. Barron, "Anti-reflection layers fabricated by a one-step copper-assisted chemical etching with inverted pyramidal structures intermediate between texturing and nanopore-type black silicon," J. Mater. Chem. A **2**, 12043 (2014).
[15] J. Yang, F. Luo, T. S. Kao, X. Li, G. W. Ho, J. Teng, X. Luo, and M. Hong, "Design and fabrication of broadband ultralow reflectivity black si surfaces by laser micro/nanoprocessing," Light: Sci. Appl. **3**, e185 (2014).
[16] K. Nishio and H. Masuda, "Anodization of gold in oxalate solution to form a nanoporous black film," Angew. Chem. Int. Ed. **50**, 1603–1607 (2011).
[17] P. B. Clapham and M. C. Hutley, "Reduction of lens reflexion by the "moth eye" principle," Nature **244**, 281–282 (1973).
[18] Y.-F. Huang, S. Chattopadhyay, Y.-J. Jen, C.-Y. Peng, T.-A. Liu, Y.-K. Hsu, C.-L. Pan, H.-C. Lo, C.-H. Hsu, Y.-H. Chang, C.-S. Lee, K.-H. Chen, and L.-C. Chen, "Improved broadband and quasi-omnidirectional anti-reflection properties with biomimetic silicon nanostructures," Nat. Nanotechnol. **2**, 770–774 (2007).
[19] H. Savin, P. Repo, G. Gastrow, P. Ortega, E. Calle, M. Garin, and R. Alcubilla, "Black silicon solar cells with interdigitated back-contacts achieve 22.1% efficiency," Nat. Nanotechnol. **10**, 624–628 (2015).
[20] R. Komatsu, A. Balčytis, G. Seniutinas, T. Yamamura, Y. Nishijima, and S. Juodkazis, "Plasmonic photo-thermoelectric energy converter with black-Si absorber," Sol. Energy Mater. Sol. Cells **143**, 72–77 (2015).
[21] G. Gervinskas, G. Seniutinas, J. S. Hartley, S. Kandasam, P. R. Stoddart, N. F. Fahim, and S. Juodkazis, "Surface-enhanced raman scattering sensing on black silicon," Ann. Phys. **525**, 907–914 (2013).
[22] E. P. Ivanova, J. Hasan, H. K. Webb, G. Gervinskas, S. Juodkazis, V. K. Truong, A. H. Wu, R. N. Lamb, V. A. Baulin, G. S. Watson, J. A. Watson, D. E. Mainwaring, and R. J. Crawford, "Bactericidal activity of black silicon," Nat. Commun. **4**, 2838 (2013).
[23] K. Tadanaga, N. Katata, and T. Minami, "Formation process of super-water-repellent Al_2O_3 coating films with high transparency by the sol–gel method," J. Am. Ceram. Soc. **80**(12), 3213–3216 (1997).
[24] A. Žukauskas, M. Malinauskas, A. Kadys, G. Gervinskas, G. Seniutinas, S. Kandasamy, and S. Juodkazis, "Black silicon: Substrate for laser 3D micro/nano-polymerization," Opt. Express **21**(6), 6901–6909 (2013).
[25] A. Balčytis, M. Ryu, G. Seniutinas, Y. Nishijima, Y. Hikima, and M. Zamengo, "Si-based infrared optical filters," Opt. Eng. **54**(12), 127103 (2015).
[26] Y. Liu, A. Das, Z. Lin, I. B. Cooper, A. Rohatgi, and C. P. Wong, "Hierarchical robust textured structures for large scale self-cleaning black silicon solar cells," Nano Energy **3**, 127–133 (2014).
[27] Z. Huang, X. Zhang, M. Reiche, L. Liu, W. Lee, T. Shimizu, S. Senz, and U. Gosele, "Extended arrays of vertically aligned sub-10 nm diameter [100] si nanowires by metal-assisted chemical etching," Nano Lett. **8**, 3046–3051 (2008).
[28] Z. Huang, N. Geyer, P. Werner, J. Boor, and U. Gosele, "Metal-assisted chemical etching of silicon: A review," Adv. Mater. **23**, 285–308 (2011).
[29] W. Wang, D. Li, M. Tian, Y. Lee, and R. Yang, "Wafer-scale fabrication of silicon nanowire arrays with controllable dimensions," Appl. Surf. Sci. **258**, 8649–8655 (2012).
[30] D. Yamaura and T. Ogino, "Fabrication of si-nanowires controlled by spontaneously formed nanoholes on annealed au thin films," Mater. Sci. Semicond. Process. **53**, 28–35 (2016).
[31] Y. Nishijima and S. Akiyama, "Unusual optical properties of the au/ag alloy at the matching mole fraction," Opt. Mater. Express **2**, 1226–1235 (2012).
[32] Y. Hashimoto, G. Seniutinas, A. Balčytis, S. Juodkazis, and Y. Nishijima, "Au-Ag-Cu nano-alloys: Tailoring of permittivity," Sci. Rep. **6**, 25010 (2016).

[33] A. J. Bett, J. Eisenlohr, O. Höhn, P. Repo, H. Savin, B. Bläsi, and J. C. Goldschmidt, "Wave optical simulation of the light trapping properties of black silicon surface textures," Opt. Express **24**(6), A434–A445 (2016).
[34] P. Spinelli, M. A. Verschuuren, and A. Polman, "Broadband omnidirectional antireflection coating based on subwavelength surface Mie resonators," Nat. Commun. **3**, 692 (2012).
[35] M. A. Green, "Self-consistent optical parameters of intrinsic silicon at 300 K including temperature coefficients," Sol. Energy Mater. Sol. Cells **92**, 1305–1310 (2008).
[36] J. Schmidt, M. Kerr, and A. Cuevas, "Surface passivation of silicon solar cells using plasma-enhanced chemical-vapour-deposited SiN films and thin thermal SiO_2/plasma SiN stacks," Semicond. Sci. Technol. **16**(3), 164–170 (2001).
[37] M. Otto, M. Kroll, T. Ksebier, R. Salzer, A. Tünnermann, and R. B. Wehrspohn, "Extremely low surface recombination velocities in black silicon passivated by atomic layer deposition," Appl. Phys. Lett. **100**, 191603 (2012).
[38] J.-W. Song, Y.-H. Nam, M.-J. Park, B. Yoo, J.-S. Cho, R. B. Wehrspohn, and J.-H. Lee, "Toward a planar black silicon technology for 50 μm-thin crystalline silicon solar cells," Opt. Express **24**(18), A1224–A1233 (2016).
[39] A. Saito, M. Yonezawa, J. Murase, S. Juodkazis, V. Mizeikis, M. Akai-Kasaya, and Y. Kuwahara, "Numerical analysis on the optical role of nanometer scale randomness on the *morpho* butterfly's scale," J. Nanosci. Nanotechnol. **11**, 2785–2792 (2011).
[40] O. Ilic, P. Bermel, G. Chen, J. D. Joannopoulos, I. Celanovic, and M. Soljačić, "Tailoring high-temperature radiation and the resurrection of the incandescent source," Nat. Nanotechnol. **11**, 320–324 (2016).